Nonresonant valence-to-core x-ray emission spectroscopy of niobium

Bruce Ravel, A. Jeremy Kropf, Dali Yang, Mengen Wang, Mehmet Topsakal, Deyu Lu,
Martin C. Stennett, and Neil C. Hyatt

Non-Resonant Valence-to-Core X-ray Emission Spectroscopy of Niobium

Bruce Ravel[*]

National Institute of Standards and Technology, Gaithersburg MD, 20899, USA

A. Jeremy Kropf and Dali Yang

Argonne National Laboratory, Argonne IL, 60439, USA

Mengen Wang

Materials Science and Engineering Department, Stony Brook University, Stony Brook NY, 11794, USA

Mehmet Topsakal and Deyu Lu

Center for Functional Nanomaterials, Brookhaven National Laboratory, Upton NY 11973, USA

Martin C. Stennett and Neil C. Hyatt

Department of Engineering Materials, The University of Sheffield,
Sir Robert Hadfield Building, Mappin Street, Sheffield, UK S1 3JD

(Dated: March 8, 2018)

The valence-to-core (V2C) portion of X-ray Emission Spectroscopy (XES) measures the electron states close to the Fermi level. These states are involved in bonding, thus provide a measure of the chemistry of the material. In this manuscript, we show the V2C XES spectra for several niobium compounds. The Kβ'' peak in the V2C XES results from the transition of a ligand $2s$ electron into the $1s$ core-hole of the niobium, a transition allowed by hybridization with the niobium $4p$. This location in energy of this weak peak shows a strong ligand dependence, thus providing a sensitive probe of the ligand environment about the niobium.

I. THE ROLE OF NON-RESONANT EMISSION SPECTROSCOPY IN STRUCTURE DETERMINATION

Synchrotron X-rays enable powerful structure determination tools, including extended X-ray-absorption fine-structure (EXAFS) analysis and scattering techniques such as Rietveld and pair distribution function analysis. While these tools contribute greatly to understanding material structures, each has its limitations. One common limitation is an insensitivity to atoms of similar atomic mass. In XAFS, the photoelectron scattering function is weakly dependent upon Z number, making it difficult to distinguish atoms with Z numbers that differ by only a few electrons. In X-ray scattering, elements of similar Z number have scattering lengths only slightly different. Even neutron diffraction is not a sure resolution to that problem. Oxygen and fluorine, for example, have very similar neutron cross sections[1]. As a result, it can be challenging to distinguish first row ligands – carbon, nitrogen, oxygen, and fluorine – in materials for which prior knowledge of the structure or composition is unavailable.

The valence-to-core (V2C) X-ray Emission Spectroscopy (XES) is a powerful complement to other structural characterization techniques. The Kβ'' XES peak arises from the transition of the ligand $2s$ electron to the $1s$ core-hole, which is made possible by hybridization, giving the ligand electron some the p character. For $3d$ metals, it is well-known[2] that this peak shows a clear dependence on ligand species. In manganese, for instance, the Kβ'' peak position changes[2] by ~ 10 eV between Mn-N and Mn-F ligands, with the peak corresponding to the more electronegative fluorine appearing at lower energy. This same ligand dependence is observed in the Kβ'' peak in other third row metals, for example titanium[3], chromium[4], iron[5], and cobalt[6].

A clear illustration of how VTC XES can resolve an otherwise ambiguous problem of structural analysis is given by the iron-molybdenum cofactor discussed in reference 5. In that work, the Fe Kβ V2C XES signal positively identifies carbon – and rules out oxygen or nitrogen – as the ligand bound to the iron atom. In that case, the identity of that ligand was unclear from XAS, vibrational spectroscopy, or other means.[7]

The $4d$ metals are found in systems of substantial scientific, technological, and economic importance. Ru, Rh, Pd, and Ag are essential to many catalytic processes. Sr, Y, Tc, and Cd are common in geochemical and environmental systems. Mo is a biologically relevant element. Ru is a component of promising light harvesting dies for artificial photosynthesis. Y, Zr, and Nb are present in certain correlated electron systems. This manuscript describes our effort to extend the use of VTC XES to the $4d$ metals.

II. XES OF 3D AND 4D METALS

Non-resonant (XES) can be a complementary measurement to X-ray absorption spectroscopy (XAS) in certain situations. Where XAS is a measure of the probability of the creation of a core-hole by an incident X-ray photon, XES measures[2] the distribution in energy of the
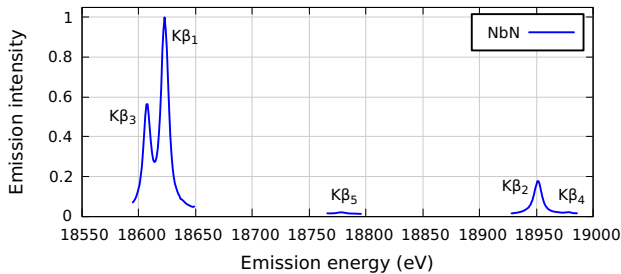
FIG. 1. Non-resonant Kβ X-ray emission spectrum for NbN. These data have been scaled such that the Kβ_1 peak is of unit height.

TABLE I. The Kβ emission lines for $4d$ transition metals, including the tabulated[9] line energies for Nb.

Line	Transition	Nb line energy
Kβ_1 / K-M$_3$	$3p_{\frac{3}{2}} \to 1s$	$18625.4\,\text{eV}$
Kβ_2 / K-N$_{2,3}$	$4p \to 1s$	$18953.4\,\text{eV}$
Kβ_3 / K-M$_2$	$3p_{\frac{1}{2}} \to 1s$	$18609.9\,\text{eV}$
Kβ_4 / K-N$_{4,5}$	$4d \to 1s$	$\approx 18982\,\text{eV}$
Kβ_5 / K-M$_{4,5}$	$3d \to 1s$	$18781\,\text{eV}$
Kβ''	ligand $2s \to 1s$	$18960\,\text{eV}$ to $18978\,\text{eV}$

secondary photon that is emitted when the core-hole is refilled. The non-resonant measurement is made with an incident photon energy well above the absorption edge energy of the target element. The valence-to-core (V2C) portion of the XES measures the transition of high-lying electrons with energies very close to the Fermi energy. The states probed by the V2C XES are states involved with bonding, therefore are sensitive to the chemistry of the absorbing atom. The non-resonant XES measurement certainly contains less information[2] about the chemical state of the material than measurements made in the resonant regime, with the incident photon energy close to the core-hole excitation energy. It is, however, a relatively simple and quick measurement that can be added to an XAFS or diffraction measure campaign at a synchrotron.

Unlike the $3d$ transition metals, the V2C Kβ emission spectroscopy of the $4d$ metals has not been extensively investigated. In a brief study[8] to assess the application of XES to the investigation of molybdenum-complex bio-chemistry, V2C XES for metallic Mo is compared to the oxide K_2MoO_4. The Kβ_2 and Kβ_4 lines are observed, with a small chemical shift in the Kβ_4 peak position. Additionally, the oxide displays a Kβ'' peak midway between the Kβ_2 and Kβ_4 that is absent from the metallic Mo spectrum. The authors attribute this to a transition from the ligand $2s$ level, the same transition as the Kβ'' in the $3d$ metals.

In this manuscript, we explore the ligand dependence of the V2C XES in a series of standard Nb compounds to show that the Kβ'' of $4d$ metals displays a similar ligand dependence as seen in the $3d$ metals. The full Nb Kβ spectrum measured from NbN is shown in Fig. 1. The energies of the various Kβ emission lines[9] for Nb are given in Table I along with their Siegbahn and IUPAC notations and electronic transitions. The data in this manuscript were measured using a recently developed, high-resolution spectrometer based on a bent Laue analyzer. All data were measured at MRCAT,[10] beamline 10ID at the Advanced Photon Source (APS), an undulator[11] beamline with a double crystal Si(111) monochromator.

III. THE BENT LAUE SPECTROMETER

Our wavelength-dispersive spectrometer uses a bent Laue analyzer[12–14] to spatially disperse photons onto an area detector, much like the instrument described in reference 15. The incident beam is focused in the Kirkpatrick-Baez geometry[16] to a spot of less than $20\,\mu m$ on the sample with flux of about 10^{12} photons/second. The analyzer is a $150\,\mu m$ thick Si(400) crystal miscut $3°$ from the surface normal. The crystal is mounted by bending over a cylindrical aluminum frame with a bend radius of $0.5\,\text{m}$. We scatter from a Si(066) reflection. The analyzer is mounted on a rotation stage at a distance of about $43\,\text{cm}$ from the sample and declined about $20°$ below the plane of the incident beam. The face of the analyzer is rotated to the angle determined by Bragg scattering from the Si(066) plane and at the energy of the emission line being measured. A Dectris Pilatus 100K area detector[17] is mounted on a rotation arm with its detecting surface facing the analyzer crystal. The area detector is rotated to twice the angle of the analyzer crystal to capture the light diffracted from the analyzer.

The band pass of the analyzer is such that, in the energy regime shown in Fig. 1, photons in a range of about $60\,\text{eV}$ disperse onto the face of the detector. While measuring within that energy range, no part of the spectrometer is in motion. The emission lines shown in Fig. 1 were measured with the Si(066) analyzer and the detector in three distinct orientations determined by Bragg's law[18] from the energies of the K$\beta_{1,3}$, Kβ_5, and K$\beta_{2,4}$ lines. Because the analyzer crystal is a thin wafer bent over the surface of a frame machined to the approximate shape of a cylinder and because the frame has a large rectangular hole beneath the middle of the crystal to allow passage of the Laue diffracted photons, the crystal is significantly distorted. As a result, the shape made by the photons dispersed onto the detector is irregular and highly dependent on subtle details of the experimental setup. An example of this peculiar shape is seen in Fig. 2A.

To interpret images like the one in Fig. 2A, we have developed an algorithm for mapping pixel to energy. Our algorithm is similar to that described in reference 20, but adapted for the peculiar shapes of these images. It requires a sequence of calibration images measured by
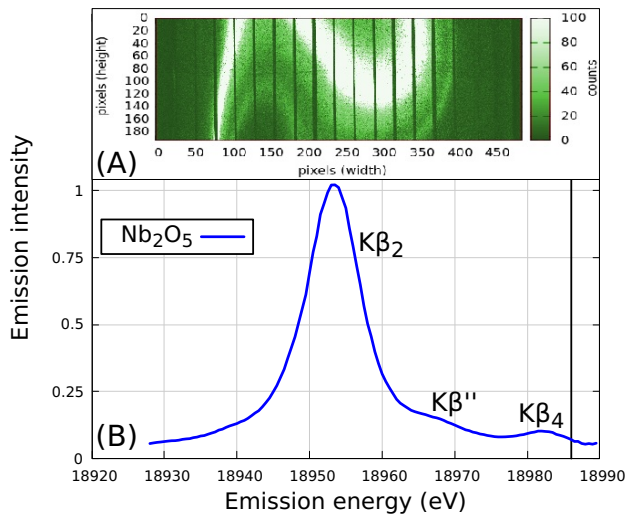
FIG. 2. Non-resonant XES data for Nb_2O_5 measured with an incident beam of 19100 eV. Part A shows the measured image for this sample. Using a sequence of calibration masks (see Fig. 3), the image is converted into the plot of XES intensity in part B. The bright portion of the image is the signal from the $K\beta_2$ emission line and the stripe below and to the right of the bright part is from the $K\beta_4$ emission line. The weak $K\beta''$ is the diffuse signal between the two lines. The vertical gaps in the XES image are the shadows of a set of tantalum Soller slits[19] used to reduce the impact of air scattering on the image. The vertical line in part B marks the absorption edge energy for zero-valent Nb, 18986 eV.

FIG. 3. Elastic peak images (left) are converted to masks (right) using the algorithm described in the text. At each energy, the mask is multiplied by an XES image (like the one in Fig. 2A) to produce the XES intensity at that energy. The vertical gaps in these images are the shadows of a set of tantalum Soller slits[19] used to reduce the effect of air scattering on the image.

scanning the energy of the incident beam through the energy range of the emission line. To calibrate the $K\beta_{2,4}$ line shown in Fig. 2, the monochromator is scanned from 18928 eV to 18989.5 eV. Because the analyzer crystal is declined about 20° below the plane of the incident beam, the elastic scatter from the sample[21] can be resolved with adequate intensity when dispersed through the analyzer onto the face of the detector. In this case, the incident beam is elastically scattered from the sample itself. This assures that the geometry of the sample relative to the rest of the spectrometer is constant throughout the calibration and measurement steps.

The monochromator is moved in 0.5 eV steps through the range of the emission line. At each step an image is measured. Five such steps are shown along the left side of Fig. 3 for the energies indicated. The signal elastically scattered from the sample is the S-shaped stripe dispersing down the face of the detector as the energy increases. This sequence of images is used to associate groups of pixels with specific energies by identifying where photons of those wavelengths strike the detector after being dispersed through the analyzer. The instrumental resolution of this arrangement is about 1.2 eV in the energy range of this measurement.

Along with the elastic scatter of interest, other, unwanted photons enter the detector. Air scatter contributes at a low level throughout the image. Occasion-

ally, a diffraction peak from the sample passes though the analyzer, as seen by the bright spot near the top of the 18950 eV image (Fig. 3C). As the absorption edge is approached, the low energy tail of the $K\beta_2$ line begins to appear, as seen at the far left starting at 18960 eV (Fig. 3E) and entering the image from the top at 18980 eV (Fig. 3I). While the human eye can readily distinguish the stripe due to the elastic scattering, some image analysis is required to automate the image processing.

To remove the background due to air scatter, we remove all pixels with a value below some low threshold, typically a few counts. Next, a 5×5 Gaussian convolution filter is passed over the entire image and pixels with a value below a second cutoff threshold are removed. This distinguishes the stripe corresponding to the elastic scatter from other stray regions with counts above the background while also filling in gaps within the stripe. These two steps alone are adequate up through about 18950 eV to produce masks like Fig. 3B and 3D. The white pixels in these mask images are set to a value of 1, the remaining pixels are set to 0.

At each energy step a mask is generated, like those

shown on the right side of Fig. 3. At each energy step, the mask is multiplied by the measured XES image, like the example in Fig. 2A. The mask, then, selects the pixels from the XES image corresponding to each energy step. All data points in Fig. 2B and Fig. 4 were generated in this way.

As the absorption edge is approached, the $K\beta_2$ fluorescence signal begins to enter the image. This is seen as a diffuse stripe on the left of the elastic peak image, as seen beginning in Fig. 2E. Near the edge, as in Fig. 2I, additional intensity enters the image from the top. This portion of the signal appears in regions which contained the elastic signal at lower energies. As the sequence of images is processes, the pixels corresponding to the lower-energy elastic signal are remembered and set to zero in the mask. In this way, the masks reject pixels illuminated by the $K\beta_2$ fluorescence signal and include pixels corresponding to the elastic signal. The processing of the non-elastic signal is clear by examining Fig. 3J, which lacks the bright regions near the left and top of Fig. 3J.

In a typical image, the peak height of the $K\beta_2$ line is about 300 counts, with an integrated area of about 35,000 counts under the $K\beta_2$ peak. For that count rate, the integrated area of the $K\beta_4$ peak is about 400 counts and the integrated area of the $K\beta''$ peak is about 250 counts.

A software package for managing and reducing data from the bent Laue spectrometer is implemented using the Perl Data Language[22] and is freely available and redistributable.[23]

IV.   XES OF NB COMPOUNDS

The non-resonant $K\beta_{2,4}$ X-ray emission spectra for $Nb^{4+}C$ and the Nb^{5+} compounds Nb_2O_5 and NbF_5 were measured with an incident energy of 19100 eV (114 eV above the tabulated Nb K edge energy of 18986 eV) and are shown in Fig. 4. Samples were prepared from commercially sourced powders, dispersed in polyethylene glycol, and pressed into pellets. In the case of NbF_5, which is aggressively hygroscopic and oxidizes upon contact with water, the sample was prepared in dry atmosphere, sealed inside several nested thermoplastic bags, and measured through the sealed bags.

As in the $3d$ metals, the position of the $K\beta''$ peak is ligand dependent, with the peak for the F ligand appearing at the lowest energy, well into the shoulder of the $K\beta_2$ peak. The measured $K\beta''$ peak positions are reported in Table II. These were determined by a Levenberg-Marquardt fit[24] to the processed data using a model consisting of Voigt functions to represent the $K\beta_2$, $K\beta_4$ and $K\beta''$ peaks. Fig. 4 has a quadratic polynomial representing air scattering and other effects removed from each spectrum. The Voight functions account for both instrumental and intrinsic broadening. An example of this fitting model applied to the Nb_2O_5 data is shown in the inset to Fig. 4. The reported peak positions are the cen-
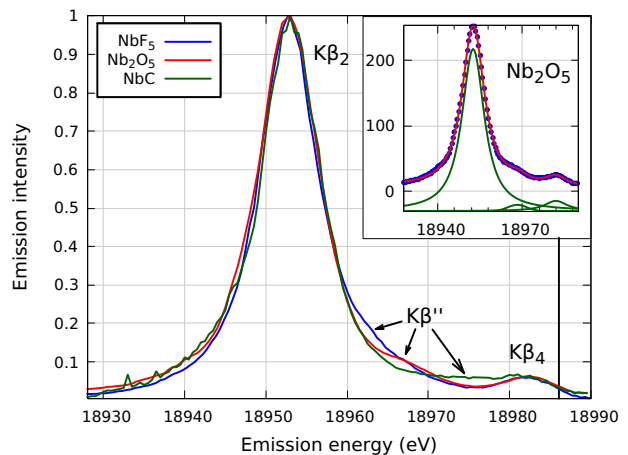
FIG. 4. Non-resonant $K\beta_{2,4}$ X-ray emission spectra for NbF_5, Nb_2O_5, and NbC. The data are shown with the background quadratics removed and scaled such that the $K\beta_2$ peaks are of unit height. The vertical line marks the absorption edge energy for zero-valent Nb, 18986 eV. The inset shows the fit to Nb_2O_5. The three fitted peak shapes, representing the $K\beta_2$, $K\beta''$, and $K\beta_4$ peaks, are shifted downward for visual clarity.

TABLE II. The $K\beta''$ line energies. The energy values of the $K\beta''$ peaks are given relative to the position of the $K\beta_2$ peak, measured experimentally at 18952.7 ± 0.3 eV. The error bars in $K\beta''$ peak position are 1σ uncertainties from the fitting procedure described in the text.

Standard	Experiment (eV)	Theory (eV)
NbF_5	8.9 ± 0.4	10.5
Nb_2O_5	15.3 ± 0.2	14.0
NbC	19.8 ± 1.3	20.3

troids of the Voight functions fitted to the $K\beta''$ peaks.

There is some variability in intensity on the low energy side of the $K\beta_2$ peak. At the lower end of the energy range, the photons diffracted by the crystal hit a narrow stripe of pixels at one edge of the crystal. Because relatively few pixels are involved in the measurement and because the signal is relatively weak, the statistical uncertainty in the measurement is higher there than elsewhere in the measurement, resulting in a noisier signal and a less certain measure of peak intensity. The NbC sample was prepared with somewhat less material than the other samples, leading to a weaker emission signal and noticeably higher shot noise in the spectrum. This is seen in Fig. 4.

V.   THEORY OF NB XES

While XAS involves transitions of core electrons to the conduction band, V2C XES concerns transitions of electrons from the valences band to the core state. Due to

the different physical processes, final state effects play different roles in XAS (core-hole) and V2C XES (valence-hole). Unlike XAS where the core-hole has large effect on the spectrum and often require explicit treatment of the electron-hole interaction, the valence-hole in XES is well screened by valence electrons. As a result, to a good approximation, XES of $1s$ emmission lines measures the projected density of states (PDOS) of valence electrons[25,26].

Projected densities of states (PDOS) of niobium compounds (NbF_5, Nb_2O_5 and NbC) were computed using the local density approximation (LDA) implemented in the QuantumESPRESSO (QE) package[27] based on crystal structures obtained from the Crystallography Open Database.[28,29] A kinetic energy (charge density) cutoff of 100 (400) Ry was used. Brillouin zone was sampled with k-point meshes of $12 \times 6 \times 6$ for NbF_5, $8 \times 2 \times 2$ for Nb_2O_5, and $18 \times 18 \times 18$ for NbC. Nb $1s$ XES spectra were calculated using the OCEAN package.[30,31] Ground state wave functions and orbital energies – the input data for OCEAN – were obtained from plane-wave, norm-conserving, pseudopotential calculations using QE. In Fig. 5, PDOS spectra have been broadened using a Gaussian function with $\sigma = 0.2$ eV and the XES spectra have been broadened by $\sigma = 1.0$ eV.

The PDOS and the OCEAN Nb K-edge V2C XES spectra of NbC, Nb_2O_5 and NbF_5 are shown in Fig. 5. The PDOS are normalized to give the Nb $4p$ PDOS unit height. Three peaks can be clearly identified, corresponding to the Nb $K\beta_2$, $K\beta''$, and $K\beta_4$ emission lines, respectively. The $K\beta_2$ line is the lowest in energy, corresponding to the Nb $4p$ PDOS, located 30 eV to 35 eV below the Fermi level. The $K\beta_4$ line is highest in energy and arises from the Nb $4d$ and ligand $2p$ hybridization that increases the dipole character of the transition, similar to the trend observed in the $K\beta_4$ lines of molybdenum compounds[8]. The dipole transition substantively dominates over the quadrupole transition, as shown for NbC in the inset to Fig. 5D, where the tiny quadrupole contribution is multiplied by 500.

The ligand $2s \rightarrow 1s$ nature of the $K\beta''$ line can be clearly seen from the corresponding ligand $2s$ PDOS. Relative to the $K\beta_2$ line, the $K\beta''$ peak positions are 10.5 eV, 14.0 eV, and 20.3 eV for NbF_5, Nb_2O_5 and NbC, respectively, in good qualitative agreement with the experimental values given in Table I. This trend can be explained by the ligand anions with larger atomic number having deeper $2s$ energy levels. The difference in the $K\beta''$ peak positions between experiment and theory can be attributed to well-known issues of the LDA functional in predicting quasi-particle energy levels. We note that the $K\beta''$ peak of NbF_5 has the highest intensity while NbC has the lowest. This can be understood as NbF_5 has the shortest average bond length of these three compounds (1.88 Å, 2.02 Å, and 2.23 Å for NbF_5, Nb_2O_5 and NbC, respectively.), increasing the spatial overlap of the Nb $2s$ with the ligand $1s$.

In order to directly compare the OCEAN calculations with the measured XES spectra, the OCEAN spectra
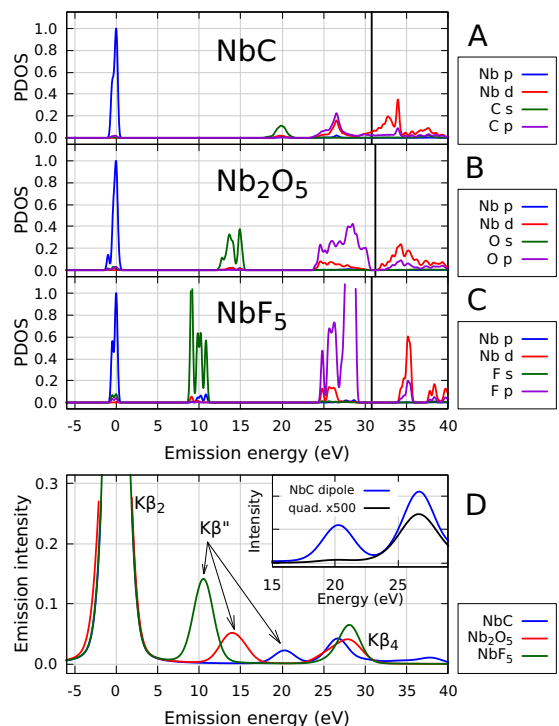
FIG. 5. Projected densities of states (PDOS) of (A) NbC (B) Nb_2O_5 and (C) NbF_5, all normalized to give unit height to the Nb $4p$ PDOS. The simulated Nb valence-to-core XES (D) of NbC (blue), Nb_2O_5 (red), and NbF_5 (green), all normalized to give unit height to the $K\beta_2$ peaks. The vertical lines in the PDOS plots indicate the positions of the Fermi level. The inset to (D) compares the dipole contribution (blue) to the quadrupole contribution (black and scaled by 500) in the XES of NbC.

were post-processed with a Gaussian broadening with $\sigma = 2.0$ eV, which is different from the value used in Fig. 5D for peak assignment. In order to consider broadening due to core hole and excited state lifetimes, an additional Lorentzian broadening was applied. We used an empirical linear function of energy[32] $\Gamma_x(E) = \alpha(E_f - E)$ as the full-width-half-maximum of the Lorentzian broadening. Here, E_f is the relative position of Fermi energy level in the XES spectrum. In previous work, $\alpha = 0.1$ was used in simulations of Si K XES.[33] For these Nb V2C XES spectra, we chose $\alpha = 0.2$. A comparison between the measured Nb_2O_5 data and the broadened spectrum is shown in Fig. 6. This broadening scheme successfully reproduces the widths of the measured peaks, although the size of the $K\beta''$ peak is somewhat overestimated.

VI. DISCUSSION

We have demonstrated a clear ligand dependence to the V2C XES of the $4d$ metal Nb. The $K\beta''$ peak, which comes from the transition of the ligand $2s$ electron to fill the Nb $1s$ core state, shifts by many eV among first-row
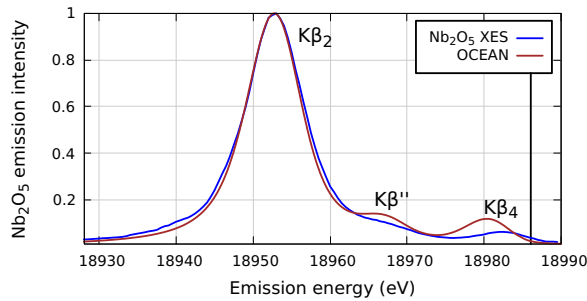
FIG. 6. The OCEAN calculation (brown) of Nb_2O_5 compared with the measured (blue) V2C XES data. The OCEAN calculation has been broadened, as explained in the text, to account for instrumental resolution as well as the lifetimes of the core-hole and excited states. Data and calculations have been normalized such that the $K\beta_2$ peak has unit height.

ligands C, O, and F – well within the detection limit of our spectrometer. The position and intensity of the $K\beta''$ is, then, a probe that can be used to positively identify the ligand species, even in situations where X-ray or neutron diffraction, XAFS, or other structural measurements cannot resolve that information.

The results of the theory shown in Fig. 5D suggest that there is a chemistry dependence in the position of the $K\beta_4$ peak. Indeed, that was seen in the earlier work on Mo.[8]

Our current spectrometer suffers from an instability that appears to be related to small temperature fluctuations in the end station. As a result, the energy axis of all XES data in this manuscript have a systematic uncertainty of a few tenths of an eV. We can clearly distinguish the positions of the $K\beta''$ peaks for the various ligands, but the chemical shifts observed in the calculations of the $K\beta_4$ peaks is close to our instrumental uncertainty. This will be the subject of future study.

[*] Corresponding author: bravel@bnl.gov

[1] V. F. Sears, Neutron News **3**, 26 (1992).

[2] P. Glatzel and U. Bergmann, Coordination Chemistry Reviews **249**, 65 (2005), synchrotron Radiation in Inorganic and Bioinorganic Chemistry.

[3] L. Mandić, S. Fazinić, and M. Jakšić, Phys. Rev. A **80**, 042519 (2009).

[4] V. A. Safonov, L. N. Vykhodtseva, Y. M. Polukarov, O. V. Safonova, G. Smolentsev, M. Sikora, S. G. Eeckhout, and P. Glatzel, The Journal of Physical Chemistry B **110**, 23192 (2006).

[5] K. M. Lancaster, M. Roemelt, P. Ettenhuber, Y. Hu, M. W. Ribbe, F. Neese, U. Bergmann, and S. DeBeer, Science **334**, 974 (2011).

[6] T.-J. Kühn, J. Hormes, N. Matoussevitch, H. Bönnemann, and P. Glatzel, Inorganic Chemistry **53**, 8367 (2014).

[7] Y. Xiao, K. Fisher, M. C. Smith, W. E. Newton, D. A. Case, S. J. George, H. Wang, W. Sturhahn, E. E. Alp, J. Zhao, Y. Yoda, and S. P. Cramer, Journal of the American Chemical Society **128**, 7608 (2006).

[8] C. J. Doonan, L. Zhang, C. G. Young, S. J. George, A. Deb, U. Bergmann, G. N. George, and S. P. Cramer, Inorganic Chemistry **44**, 2579 (2005).

[9] W. Elam, B. Ravel, and J. Sieber, Radiation Physics and Chemistry **63**, 121 (2002), *Note that line energies for Nb $K\beta_4$ and $K\beta''$ are not included in this tabulation.*

[10] C. U. Segre, N. E. Leyarovska, L. D. Chapman, W. M. Lavender, P. W. Plag, A. S. King, A. J. Kropf, B. A. Bunker, K. M. Kemner, P. Dutta, R. S. Duran, and J. Kaduk, AIP Conference Proceedings **521**, 419 (2000).

[11] Z. Cai, R. J. Dejus, P. D. Hartog, Y. Feng, E. Gluskin, D. Haeffner, P. Ilinski, B. Lai, D. Legnini, E. R. Moog, S. Shastri, E. Trakhtenberg, I. Vasserman, and W. Yun, Review of Scientific Instruments **67**, 3348 (1996).

[12] Z. Zhong, L. D. Chapman, B. A. Bunker, G. B. Bunker, R. Fischetti, and C. U. Segre, Journal of Synchrotron Radiation **6**, 212 (1999).

[13] A. J. Kropf, R. J. Finch, J. A. Fortner, S. Aase, C. Karanfil, C. U. Segre, J. Terry, G. Bunker, and L. D. Chapman, Review of Scientific Instruments **74**, 4696 (2003).

[14] A. J. Kropf, J. A. Fortner, R. J. Finch, J. C. Cunnane, and C. Karanfil, Physica Scripta **2005**, 998 (2005).

[15] N. Hiraoka, H. Fukui, H. Tanida, H. Toyokawa, Y. Q. Cai, and K. D. Tsuei, Journal of Synchrotron Radiation **20**, 266 (2013).

[16] P. Kirkpatrick and A. V. Baez, J. Opt. Soc. Am. **38**, 766 (1948).

[17] Any mention of commercial imaging or software products is for information only; it does not imply recommendation or endorsement by the National Institute of Standards and Technology.

[18] W. H. Bragg and W. L. Bragg, Proceedings of the Royal Society of London A: Mathematical, Physical and Engineering Sciences **88**, 428 (1913).

[19] W. Soller, Phys. Rev. **24**, 158 (1924).

[20] J. I. Pacold, J. A. Bradley, B. A. Mattern, M. J. Lipp,

G. T. Seidler, P. Chow, Y. Xiao, E. Rod, B. Rusthoven, and J. Quintana, Journal of Synchrotron Radiation **19**, 245 (2012).

[21] B. Dickinson, G. T. Seidler, Z. W. Webb, J. A. Bradley, K. P. Nagle, S. M. Heald, R. A. Gordon, and I. M. Chou, Review of Scientific Instruments **79**, 123112 (2008).

[22] P. Glazebrook and F. Economou, Dr. Dobb's Journal (1997).

[23] BLA-XANES, "A prototype framework for obtaining XANES and XES spectra from a bent Laue analyzer and a Pilatus detector," `https://github.com/bruceravel/BLA-XANES/` (2017), accessed 30 May, 2017.

[24] M. Wojdyr, Journal of Applied Crystallography **43**, 1126 (2010).

[25] F. de Groot, Chemical Reviews **101**, 1779 (2001).

[26] J. J. Kas, K. Jorissen, and J. J. Rehr, "Real-space multiple-scattering theory of x-ray spectra," in *X-Ray Absorption and X-Ray Emission Spectroscopy* (John Wiley & Sons, Ltd, 2016) pp. 51–72.

[27] P. Giannozzi, S. Baroni, N. Bonini, M. Calandra, R. Car, C. Cavazzoni, D. Ceresoli, G. L. Chiarotti, M. Cococcioni, I. Dabo, *et al.*, Journal of physics: Condensed matter **21**,

395502 (2009).

[28] S. Gražulis, A. Daškevič, A. Merkys, D. Chateigner, L. Lutterotti, M. Quiros, N. R. Serebryanaya, P. Moeck, R. T. Downs, and A. Le Bail, Nucleic Acids Research **40**, D420 (2012).

[29] Crystallography Open Database (COD), `http://www.crystallography.net/cod/cif/1/53/59/1535949.cif`, `http://www.crystallography.net/cod/cif/1/52/87/1528723.cif`, `http://www.crystallography.net/cod/cif/9/00/86/9008682.cif` (2017), accessed 30 May, 2017.

[30] J. Vinson, J. J. Rehr, J. J. Kas, and E. L. Shirley, Physical Review B **83**, 115106 (2011).

[31] K. Gilmore, J. Vinson, E. L. Shirley, D. Prendergast, C. D. Pemmaraju, J. J. Kas, F. D. Vila, and J. J. Rehr, Computer Physics Communications **197**, 109 (2015).

[32] C. Hébert, Micron **38**, 12 (2007).

[33] P. J. W. Weijs, M. T. Czyzyk, J. F. van Acker, W. Speier, J. B. Goedkoop, H. van Leuken, H. J. M. Hendrix, R. A. de Groot, G. van der Laan, K. H. J. Buschow, G. Wiech, and J. C. Fuggle, Phys. Rev. B **41**, 11899 (1990).